



# Amplification-Free SARS-CoV-2 Detection Using Nanoyeast-scFv and Ultrasensitive Plasmonic Nanobox-Integrated Nanomixing Microassay

Junrong Li, Alain Wuethrich,\* Selvakumar Edwardraja, Richard J. Lobb, Simon Puttick, Stephen Rose, Christopher B. Howard,\* and Matt Trau\*



Cite This: *Anal. Chem.* 2021, 93, 10251–10260



Read Online

ACCESS |



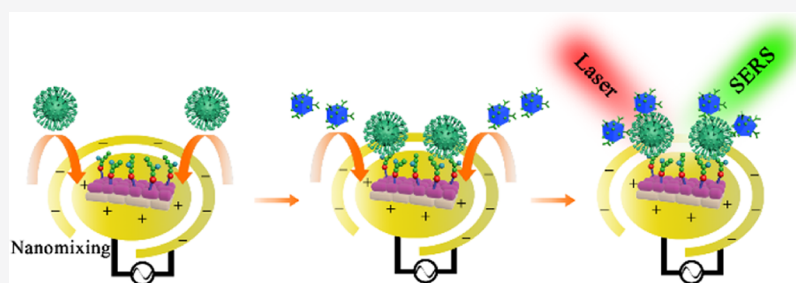
Metrics & More



Article Recommendations



Supporting Information



**ABSTRACT:** The implementation of accurate and sensitive molecular detection for the severe acute respiratory syndrome coronavirus 2 (SARS-CoV-2) is paramount to effectively control the ongoing coronavirus disease 2019 (COVID-19) pandemic. In this regard, we herein propose the specific and highly sensitive SARS-CoV-2 detection based on nanoyeast single-chain-variable fragment (scFv) and ultrasensitive plasmonic nanobox-integrated nanomixing microassay. Importantly, this designed platform showcases the utility of nanoyeast-scFvs as specific capture reagents targeting the receptor-binding domain (RBD) of the virus and as monoclonal antibody alternatives suitable for cost-effective mass production and frequent testing. By capitalizing on single-particle active nanoboxes as plasmonic nanostructures for surface-enhanced Raman scattering (SERS), the microassay utilizes highly sensitive Raman signals to indicate virus infection. The developed microassay further integrated nanomixing for accelerating molecular collisions. Through the synergistic working of nanoyeast-scFv, plasmonic nanoboxes, and nanomixing, the highly specific and sensitive SARS-CoV-2 detection is achieved as low as 17 virus/ $\mu\text{L}$  without any molecular amplification. We successfully demonstrate SARS-CoV-2 detection in saliva samples of simulated patients at clinically relevant viral loads, suggesting the possibility of this platform for accurate and noninvasive patient screening.

Since the World Health Organization (WHO) announced the coronavirus disease 2019 (COVID-19) as a global pandemic, the severe acute respiratory syndrome coronavirus 2 (SARS-CoV-2) has resulted in more than 126 million confirmed cases and over 2 million deaths globally,<sup>1</sup> which has largely overwhelmed the modern health care systems in some countries. As the SARS-CoV-2 is highly contagious, the isolation and quarantine of symptomatic individuals are key regulation measures to mitigate the community transmission. Nevertheless, the displayed symptoms (e.g., cold, fever, and headache) are not unique to SARS-CoV-2 infection and individuals can be infectious several days before they show clinical symptoms, which poses an immense challenge to identify patients to eliminate viral transmission.<sup>2,3</sup> In addition, a proportion of asymptomatic individuals with SARS-CoV-2 infection still carries a high risk of virus transmission, thereby escalating the threats in the ongoing pandemic.<sup>3,4</sup> To minimize virus propagation and effectively control the current, or future pandemics, the development of molecular diagnostic assays to

specifically identify SARS-CoV-2 is essential for an early, timely, and accurate screening of COVID-19 patients.<sup>5,6</sup>

The ability to perform molecular tests for SARS-CoV-2 provides the scientific evidence for mandatory quarantine.<sup>5</sup> Currently, the prevalent gold standard molecular diagnosis of SARS-CoV-2 is viral RNA detection using quantitative reverse transcription polymerase chain reaction (RT-qPCR).<sup>7</sup> The viral RNA-based amplification strategy for SARS-CoV-2 detection has also been employed in the popular clustered regularly interspaced short palindromic repeats (CRISPR) technique.<sup>8–11</sup> Despite the superior sensitivity ( $\sim 1$  copies/ $\mu\text{L}$ )

Received: April 19, 2021

Accepted: July 6, 2021

Published: July 15, 2021



in patient screening,<sup>12</sup> these viral RNA amplification assays have the limitations of the necessity to extract RNA from the biological samples and the potential bias introduced during target amplification. As an alternative to viral RNA detection, the protein-based lateral flow assay has been introduced to detect the viral antigens<sup>13</sup> or virus-specific antibodies (e.g., IgG and IgM),<sup>14–16</sup> allowing rapid and point-of-care screening via lateral flow assay. However, the protein-based assay often relies on the use of monoclonal antibodies. The production of monoclonal antibodies is relatively expensive, time-consuming, and can suffer from batch-to-batch variability.<sup>17,18</sup> A key issue of the current antigen tests is less sensitive than PCR tests, hence limiting their use in the field of accurate patient screening.<sup>19</sup> The serological detection of virus-specific antibodies is problematic due to the long time needed for patients to generate antibodies following symptom onset, which can increase the risk of disease spreading.<sup>8,20</sup>

To effectively facilitate the patient screening for this pandemic, an ideal SARS-CoV-2 detection platform should fulfill the following criteria: (1) enabling the detection with minimal sample pretreatment and without amplification to avoid bias; (2) employing cost-effective and stable probes that should be suitable for mass production and thereby permitting frequent tests; and (3) sensitive and real-time reflecting viral loads to allow an early response to infectious cases. We herein report a nanoyeast single-chain variable fragment (scFv) and ultrasensitive plasmonic nanobox-integrated nanomixing microassay for SARS-CoV-2 detection. In the designed platform, the virus is detected from diluted saliva samples without any sample preparation. The amplification-free and accurate detection is achieved via surface-enhanced Raman scattering (SERS) assisted by nanomixing, in which the single-particle active gold–silver alloy nanoboxes significantly amplify the Raman signal readout and nanomixing further enhances the mass transfer for higher sensitivity.<sup>21–23</sup> Critically, we designed and engineered scFvs on nanoyeasts as reproducible high-affinity probes targeting and identifying the receptor-binding domain (RBD) of the virus. As detection does not rely on virus-specific antibodies, the platform is expected to rapidly indicate virus infection and lower the risk of virus transmission. Our assay is capable of detecting as low as 17 virus/ $\mu\text{L}$  and identifying simulated COVID-19 saliva patient samples, providing a potential strategy for early SARS-CoV-2 diagnosis. In comparison to assays that rely on monoclonal antibodies for viral antigen capture, the nanoyeast-scFvs allow inexpensive mass production within a fast turnaround time (about 2 weeks), thus providing the possibility for population-level screening.<sup>24,25</sup> Furthermore, the developed assay with PCR-comparable sensitivity enables more accurate detection than the rapid antigen test.

## ■ EXPERIMENTAL SECTION

### Engineering and Production of Nanoyeast-scFvs.

Yeast cells were bioengineered to display proteins on the yeast cell surface targeting the SARS-CoV-2 spike protein. This surface display was achieved by fusing these proteins to the C-terminus of the yeast surface adhesion protein Aga2p, which interacts with the cell surface anchor Aga1p. To achieve cell surface display, gene sequences encoding antibody fragments targeting SARS-CoV-2 including S309, the SARS-CoV cell receptor ACE2, and antibody fragments targeting SARS-CoV-1 and Dengue virus targets were synthesized by Genent (Thermo). Each sequence was codon-optimized for protein

expression in the yeast *Saccharomyces cerevisiae*, and *Nhe1* and *Sal1* restriction enzyme sites were incorporated into the gene construct design to enable cloning of genes into the yeast surface to display expression DNA plasmid vector pCTCON2. pCTCON2 was kindly provided by the National Biologics Facility, AIBN, and was initially sourced from the lab of Dane Wittrup via Addgene: Plasmid #41843. In the pCTCON2 vector, the genes were cloned at the C-terminus of the yeast cell surface protein Aga2p. This enables the display of proteins on the surface of the yeast via the fusion partner Aga2p protein, which interacts via a disulfide bridge with another anchor protein Aga1p. A c-myc peptide tag was included at the C-terminus of each gene construct to enable the detection of expressed proteins. There was also a hemagglutinin (HA) peptide tag at the C-terminus of the Aga2p fusion protein for the detection of the Aga2p fusion protein. For the expression of proteins on the surface of yeast, the gene constructs in pCTCON2 were transformed into the EBY100 strain of *S. cerevisiae* yeast cells following the previous work.<sup>26</sup> Briefly, 10  $\mu\text{L}$  of recombinant DNA (1000 ng) was transformed into competent EBY100 yeast cells grown in YPD media using electroporation (Gene Pulser Xcell Electroporation, BioRad) with a square-wave protocol of 1 pulse only at 500 V for 15 ms in a 4 mm glass cuvette. The transformed yeast cells were selected in the SDCAA yeast medium and grown at 30° overnight to an OD<sub>600</sub> of 5–10. The SDCAA culture was diluted to an OD<sub>600</sub> of 0.5–1.0 in the SGCAA induction medium containing galactose and induced at 30 °C for 48 h. The OD<sub>600</sub> reached was 6–10. The cell surface expression of the Aga2p fusion proteins in SGCAA cultures was confirmed by flow cytometry.

For the preparation of nanoyeast, a 25 mL culture of SGCAA yeast was prepared to an OD<sub>600</sub> of 6–10. The yeast was collected and washed by centrifugation at 2000g for 10 min. The centrifuged product was resuspended in 10 mL of chilled 1× phosphate-buffered saline (PBS) supplemented with 1 tablet of Protease Inhibitor Cocktail with EDTA (Roche). The cells were stored on ice and sonicated 1 min on/1 min off using the Sonics Ultra Processor VC-505 sonicator. The sonication instrument was set to 40% amplitude, ultrahigh intensity using a 3 mm tip diameter and 171 mm length. This process was repeated five times. Following sonication, the sample was centrifuged at 2000g for 10 min and the supernatant was kept and filtered through a 0.1  $\mu\text{m}$  filter unit (Millipore) to get the final nanoyeast products.

**Synthesis of Gold–Silver Alloy Nanobox-Based SERS Nanotags.** The nanoboxes were synthesized first prior to the co-functionalization with 2,7-mercapto-4-methylcoumarin (MMC) Raman reporter and polyclonal anti-RBD antibodies. The preparation of nanoboxes follows our previous work.<sup>27</sup>

The prepared nanoboxes were functionalized with MMC and antibodies through gold-thiol and 1-ethyl-3-(3-dimethylaminopropyl)carbodiimide (EDC)/*N*-hydroxysuccinimide (NHS) chemistry, respectively. First, 300  $\mu\text{L}$  of nanoboxes concentrated from 1 mL of solution with the centrifugation at 800g for 15 min were incubated with 10  $\mu\text{L}$  of MMC (1 mM) and 2  $\mu\text{L}$  of MUA (1 mM) for 6 h. After centrifuging the nanoboxes to remove free MMC and MUA, 10  $\mu\text{L}$  of EDC (10 mM) and 20  $\mu\text{L}$  of Sulfo-NHS (10 mM) were added and incubated at 25 °C, 350 rpm for 30 min to activate the carboxyl groups on MUA. Subsequently, the nanoboxes were centrifuged at 800g for 15 min to remove the excess amount of EDC and Sulfo-NHS. Finally, 0.5  $\mu\text{L}$  of

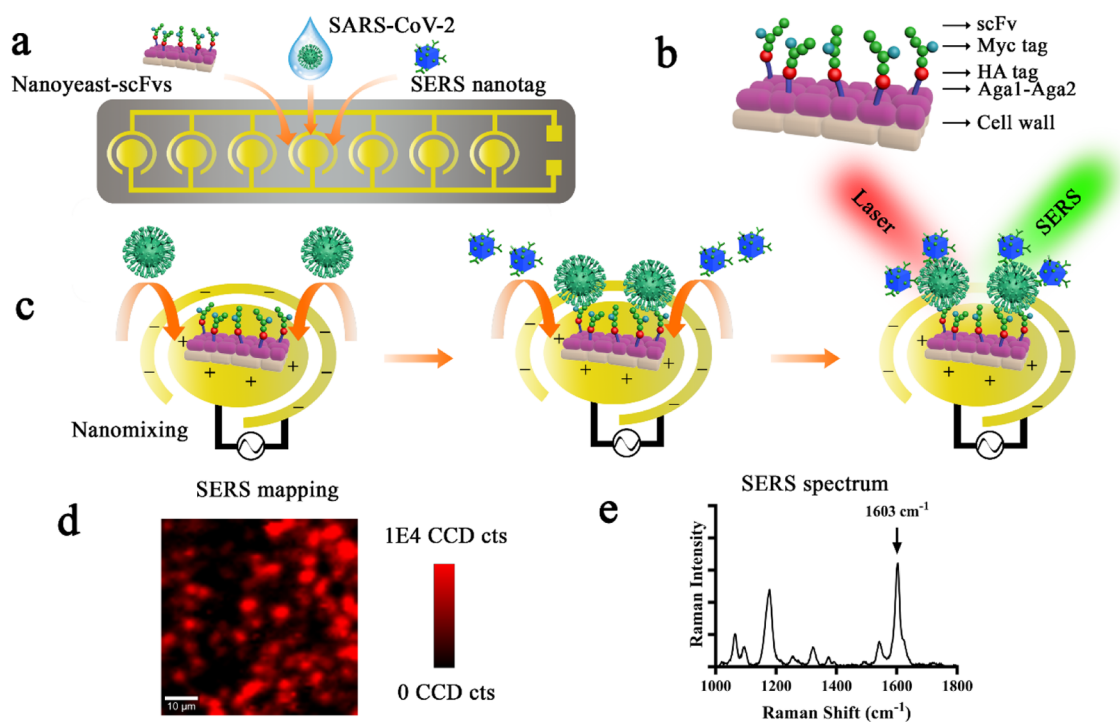


**Figure 1.** Workflow of SARS-CoV-2 detection on the nanoyeast-scFv and ultrasensitive plasmonic nanobox-integrated nanomixing microassay. Schematic illustration of (a) gold microelectrodes as reaction chambers for parallel detection of SARS-CoV-2 and (b) the structure of nanoyeast-scFv fragments. (c) Stepwise reactions on the microelectrodes, including the specific capture of virus by nanoyeast-scFvs, labeling the virus with SERS nanotags, and Raman mapping for signal readout. (d) Representative SERS mapping image from the microelectrodes and (e) the extracted average SERS spectrum from the Raman image.

polyclonal antibodies were added into the solution and incubated at 25 °C, 350 rpm for 30 min, followed by removing the free antibodies through centrifugation and blocking the surface with 200  $\mu$ L of 0.1% bovine serum albumin (BSA).

**Gold Microelectrode Array Fabrication and Functionalization.** The gold microelectrode array was fabricated on a 4-inch glass substrate by photolithography.<sup>28</sup> For the functionalization, S309 nanoyeast-scFvs were conjugated to the gold microelectrode array via affinity pull down using anti-HA antibody. A solution of 4 mg/mL dithiobis(succinimidyl propionate) (DSP) in dimethyl sulfoxide was incubated on the gold electrodes for 30 min at room temperature. After three washes with ethanol and 1 $\times$  PBS, a solution of 10  $\mu$ g/mL anti-HA antibody in 1 $\times$  PBS was incubated for 2 h at room temperature. The microelectrode arrays were then washed with 1 $\times$  PBS and incubated overnight at 4 °C with S309 nanoyeast-scFvs (protein concentration:  $\sim$ 3 mg/mL). The microelectrode array functionalization was completed by a blocking step with 3% BSA for 1 h at room temperature.

**Detecting RBD, SARS-CoV-2, or Simulated COVID-19 Patients on the Nanoyeast-scFv-Integrated Nanomixing SERS Microarray Platform.** RBD and SARS-CoV-2 samples were prepared by diluting stock solutions of RBD (5  $\mu$ g/mL) and SARS-CoV-2 ( $2 \times 10^{10}$  virus/mL) in 1 $\times$  PBS to the desired concentration. Simulated patient saliva samples were prepared by spiking designated virus concentrations into five fold diluted healthy saliva (diluted with 1 $\times$  PBS). The sample (50  $\mu$ L) was incubated in each well of the microelectrode array for 45 min under an applied alternating current electrohydrodynamic (ac-EHD) field of 500 Hz and 800 mV to stimulate nanoscopic mixing. After RBD or SARS-CoV-2 capture, 30  $\mu$ L of the SERS nanotag solution was added

for labeling under nanoscopic mixing for 20 min using the same ac-EHD field conditions as above. Subsequently, excess SERS nanotag solution was removed from the wells. The wells were washed three times with 1 $\times$  PBS before first use of the microelectrode array and after each incubation step. All steps were performed at room temperature.

**Culture of SARS-CoV-2 in Cell Line.** The culture of SARS-CoV-2 and preparation of  $\gamma$  irradiated stocks were performed by researchers at the Australian Centre for Disease Preparedness (ACDP), CSIRO, Geelong. The SARS-CoV-2 was obtained by infecting the VeroE6 (ECACC) cells in a biosafety level 3 laboratory. The VeroE6 cells were cultured in Dulbecco's modified Eagle's medium (DMEM) with 2% fetal bovine serum and inoculated with viral inoculum when the cells reached 70–90% confluence. The inoculated flasks were then incubated at  $37 \pm 2$  °C with a  $5 \pm 2\%$  CO<sub>2</sub> incubator. Virus in the supernatant were harvested and clarified by centrifugation at 4500g for 10 min. To inactivate the virus,  $\gamma$  irradiation at a dose of 50 kGy was applied to virus.

## RESULTS AND DISCUSSION

**Working Principle of SARS-CoV-2 Detection.** Figure 1 depicts the schematic workflow of amplification-free SARS-CoV-2 detection by the nanoyeast-scFv and ultrasensitive plasmonic nanobox-integrated nanomixing microassay. We fabricated a microarray platform with multiple asymmetrical gold microelectrodes on the glass substrate and performed SARS-CoV-2 detection using microelectrodes as reaction chambers (Figure 1a). Specifically, nanoyeast-scFvs were utilized to capture SARS-CoV-2, followed by reading out amplified Raman signals from nanobox-based SERS nanotags on microelectrodes. By applying an alternating current

electrohydrodynamic (ac-EHD) on the asymmetrical micro-electrodes, a nanoscaled force (i.e., nanomixing) was created within the two nonuniformly charged double layers, which was able to drive the mixing of molecules in solution to enhance mass transfer and binding efficiency for higher sensitivity and specificity.<sup>21–23</sup>

First, we engineered a panel of yeast displaying proteins such as scFvs that specifically target the RBD on SARS-CoV-2. The use of yeast cells to engineer scFvs has the advantages of streamlined genetic engineering to produce A-agglutinin anchorage (Aga)-linked scFvs that are stable under various conditions (e.g., ionic strength and temperature).<sup>24</sup> In addition, yeast scFvs can be produced via a cost-effective, simple, and animal-free method.<sup>29,30</sup> To suit the miniaturized needs of biological application and maintain activity and stability, we produced nanoyeast-scFvs via mechanical fragmentation of the intact yeast cells. As shown in Figure 1b, scFvs were designed to be covalently linked on yeast cell walls via the Aga subunits 1 and 2, which provided the necessary binding flexibility for scFvs. Furthermore, to enable the subsequent characterization, functionalization, or labeling of the nanoyeasts, we introduced human influenza hemagglutinin (HA) and myc peptide tags together with scFvs. In comparison to the tedious and time-consuming production of monoclonal antibodies, nanoyeast-scFvs offer similar binding avidity by a streamlined and rapid production (i.e., 2–3 weeks) that is suitable for mass production.<sup>24,25</sup> We have demonstrated the applications of nanoyeast-scFvs as antibody alternatives in cancer biomarker detection.<sup>25,27</sup> Here, we further extended the utility of nanoyeast-scFvs as affinity reagents in infectious disease. Under the assistance of nanomixing, the newly generated nanoyeast-scFvs were able to effectively capture SARS-CoV-2 in biological samples by binding with the RBD on the viral surface.

Following the nanoyeast-scFv capture of virus on gold microelectrodes, SERS nanotags were subsequently applied on the microarray under nanomixing to identify and detect SARS-CoV-2 (Figure 1c). Particularly, the prepared SERS nanotags were composed of gold–silver alloy nanoboxes co-functionalized with Raman reporters (i.e., MMC) and anti-RBD polyclonal antibodies, in which nanoboxes acted as plasmonic nanostructures to amplify the Raman reporter signals for readout and the polyclonal antibodies guided the nanoboxes toward SARS-CoV-2. To this end, the SERS mapping image was expected to show identifiable and characteristic Raman signals from SERS nanotags at 1603  $\text{cm}^{-1}$  (Figure 1d). As the virus concentration was positively correlated to the bound SERS nanotag amounts, the quantity of virus can be inferred from the average Raman intensities at 1603  $\text{cm}^{-1}$  of SERS spectra (Figure 1e).

By leveraging the high specificity and affinity of nanoyeast-scFvs to SARS-CoV-2, the current platform exhibited the advantages of directly detecting SARS-CoV-2 without any molecular amplification because of the single-particle SERS activity of the as-prepared nanoboxes,<sup>31</sup> the intrinsic high sensitivity of SERS,<sup>32,33</sup> and the enhanced mass transfer contributed by nanomixing.<sup>21,22,34</sup> To demonstrate the benefit of nanomixing, we compared the RBD detection with and without nanomixing. As shown in Figure S1, the use of nanomixing enhanced about 8.8 times SERS signals in comparison to the detection without nanomixing, which suggested the increased sensitivity contributed by nanomixing.

### Screening for High-Affinity Nanoyeast-scFv Probes.

Given the high specificity and sensitivity required to detect the virus, we applied the yeast display technology to genetically engineer yeast cells to display the scFvs (i.e., S309,<sup>35</sup> COVA1–12,<sup>36</sup> COVA2–07,<sup>36</sup> COVA2–04,<sup>36</sup> CR3022,<sup>37</sup> and cell receptor ACE2<sup>38</sup>) that were reported to bind to RBD but may have diverse affinity or expression levels on yeast cells. The fragmented nanoyeast-scFvs were functionalized on the microarray via attaching the HA tag of nanoyeasts with HA antibodies on gold microelectrodes. Using these nanoyeast-scFvs as capturing probes for RBD on the designed platform, Figure 2 shows the average Raman intensities at 1603  $\text{cm}^{-1}$

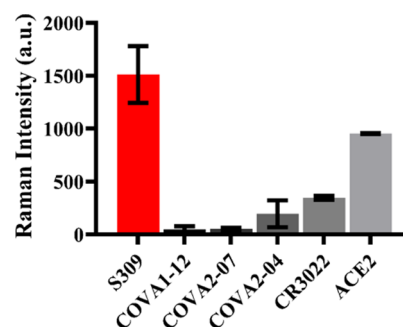


**Figure 2.** Screening of nanoyeast-scFvs for highly sensitive RBD detection. The average Raman intensities at 1603  $\text{cm}^{-1}$  using different nanoyeast-scFvs to capture soluble RBD (500 ng/mL). Error bars indicate the standard error of three replicates.

from the SERS mapping images for comparison. As expected, different Raman intensities were obtained from these nanoyeast-scFvs, in which S309 nanoyeast-scFvs generated the strongest signals. As such, S309 nanoyeast-scFvs were selected as the probes for targeting RBD in the SARS-CoV-2 detection.

**S309 scFv Expression Levels and Binding Affinity toward RBD.** As S309 has the best performance among the panel of engineered scFvs, we profiled the S309 scFv display levels on yeast cells and determined the binding affinity to RBD, which are critical to the virus detection. The yeast cells engineered to display S309 scFvs were then labeled with both anti-myc-Dy650 and RBD-mNeonGreen fluorescent protein for the flow cytometry analysis. As shown in Figure 3a, the yeast cells demonstrate the S309 expression and capability of binding to RBD with a high percentage of 57.91% in the total

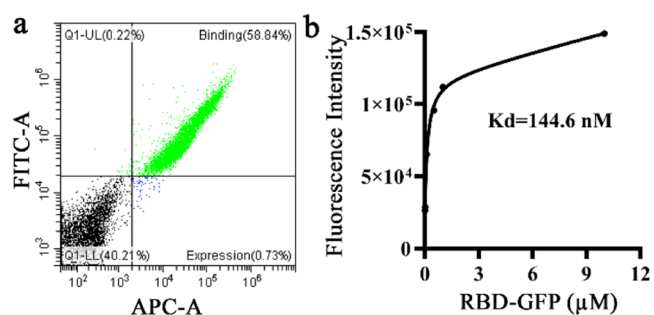


**Figure 3.** Flow cytometry profiling of S309 scFv display level and the determination of RBD binding affinity. Yeast cells were labeled with anti-myc-Dy650 and RBD-mNeonGreen. (a) S309 scFv display level and the binding of RBD and (b) plot of mean fluorescence intensity with different RBD concentrations for calculating RBD binding affinity.

yeast cell population. To calculate the S309 scFv binding affinity toward RBD, the yeast cells were incubated with designated concentrations of RBD-mNeonGreen (Figure S2). Based on the obtained mean fluorescence intensities, the determined binding affinity of S309 scFvs to RBD was in the nanomolar range (i.e.,  $K_d = 144.6$  nM) (Figure 3b), which was comparable to the reported monoclonal S309 antibodies.<sup>35</sup> The successful expression of S309 and the corresponding high binding affinity underpinned the highly sensitive RBD and SARS-CoV-2 detection of the generated nanoyeast-scFvs.

**Characterization of S309 Nanoyeast-scFv and Nanoboxes.** Having demonstrated the expression and high affinity of S309 scFvs on yeast cells, we then performed the physical characterization of these nanoscopic bodies. The size of the S309 nanoyeast-scFvs was characterized by nanoparticle tracking analysis (NTA) that allows the real-time tracking of individual particles. As shown in Figure 4a, the S309

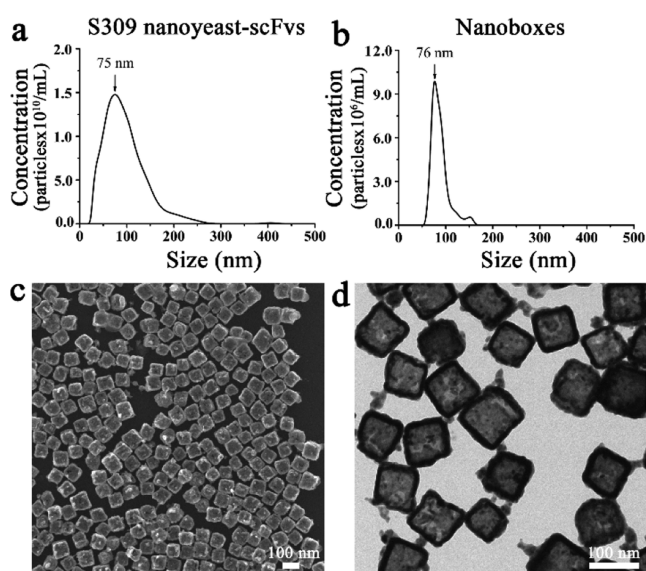


**Figure 4.** S309 nanoyeast-scFv and nanobox physical characterization. The size distribution of (a) S309 nanoyeast-scFvs and (b) nanoboxes; (c) scanning electron microscope (SEM) and (d) transmission electron microscope (TEM) images of nanoboxes.

nanoyeast-scFvs have a mode size of  $74.0 \pm 4.2$  nm with a relatively broad size distribution probably due to the inhomogeneous fragmentation of yeast cells. In addition, the size of the S309 nanoyeast-scFvs was further analyzed with nanoflow cytometry measurement system (Figure S3), which demonstrated a slightly smaller mode size of  $62.0 \pm 1.5$  nm.

To characterize the size and morphology of as-prepared gold–silver alloy nanoboxes, we performed NTA, scanning electron microscopy (SEM), and transmission electron microscopy (TEM). NTA indicated that nanoboxes had a similar mode size (76 nm) compared to nanoyeast, but nanoboxes displayed a narrower size distribution (Figure 4b). The SEM image (Figure 4c) and TEM image (Figure 4d) demonstrated that the nanoboxes had a uniform size of around 80 nm. The stark contrast in TEM image also indicated the hollow inner structure of the nanoboxes with a wall thickness of around 15 nm. As the size of nanoboxes was within the optimal range (30–100 nm) for Raman signal enhancement, the use of single-particle active nanoboxes as SERS plasmonic

nanostructures can achieve ultrasensitive signal readout for SARS-CoV-2 detection.<sup>39</sup>

**Microelectrode Array Functionalization with S309 Nanoyeast-scFvs.** Aiming for the optimal performance, we evaluated and compared two strategies of functionalizing S309 nanoyeast-scFvs on microelectrode surfaces for soluble RBD detection. S309 nanoyeast-scFvs were attached to the microelectrodes through either physisorption or specific surface immobilization via anti-HA antibody binding to the engineered HA tag on nanoyeasts. To allow the HA tag-assisted nanoyeast-scFv functionalization, the microelectrodes were first labeled with anti-HA antibodies via dithiobis(succinimidyl propionate) (DSP) linker prior to capturing nanoyeasts through the HA tag.

As demonstrated by the result of soluble RBD detection in Figure 5a, the physisorption of S309 nanoyeast-scFvs on

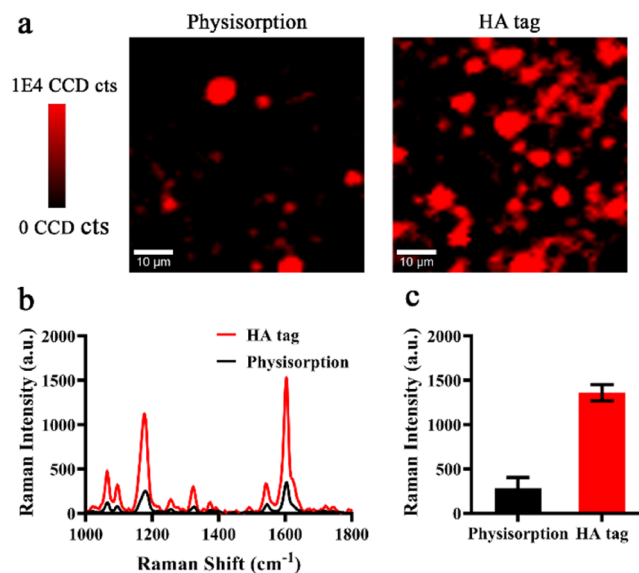


**Figure 5.** Functionalization of the gold microelectrode array via physisorption or HA tag surface immobilization method. SERS mapping image of detecting soluble RBD with (a) physisorption and HA tag method, (b) the corresponding average Raman spectra, and (c) Raman intensity at  $1603$   $\text{cm}^{-1}$ .

microelectrodes generated weaker Raman signal distribution, whereas the HA tag-assisted S309 nanoyeast-scFv functionalization produced uniform and widespread Raman signals. In agreement with the SERS mapping images, the extracted average Raman spectrum from nanoyeast-scFv physisorption displayed much weaker signals than the HA-tag-based functionalization strategy (Figure 5b). Based on the Raman intensity at  $1603$   $\text{cm}^{-1}$ , the HA tag-assisted S309 nanoyeast-scFv binding displayed around 5 times higher signal than the simple physisorption (Figure 5c). The enhanced performance of HA tag-assisted functionalization was probably due to the increased binding efficiency of nanoyeasts towards microelectrodes and the selective binding of nanoyeasts that displayed scFvs. As a result, we opted for utilizing HA tag engineered on nanoyeasts to functionalize microelectrodes for sensitive readout.

Additionally, we evaluated the reproducibility of HA tag-assisted surface functionalization by measuring SERS signals on different microelectrodes in the detection of RBD. As shown in Figure S4, the relatively uniform SERS signals among

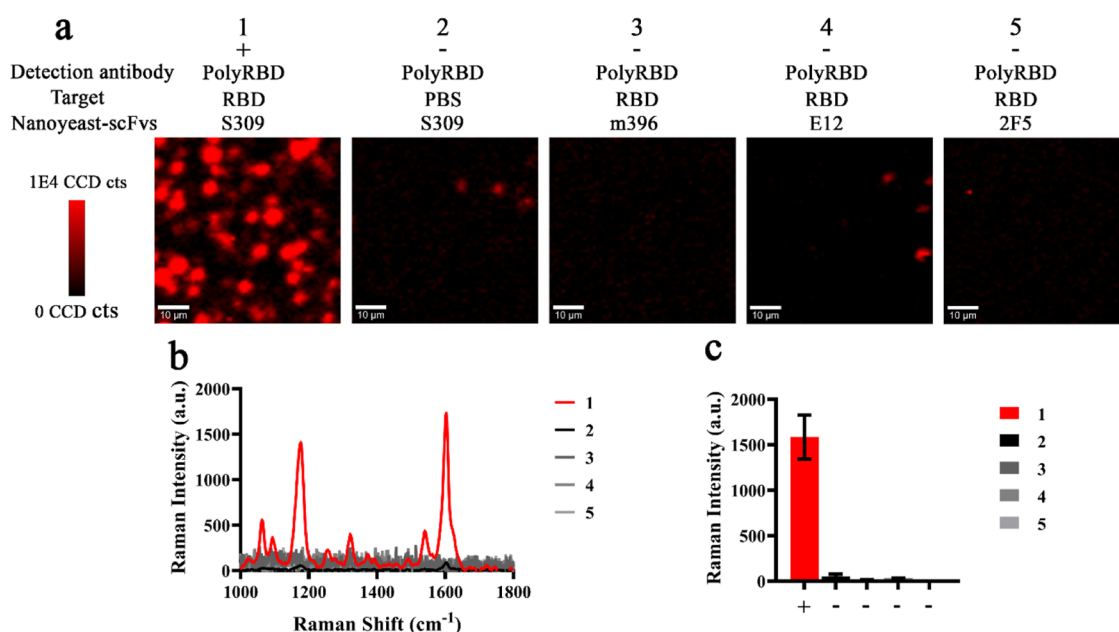


**Figure 6.** Specificity study for the detection of soluble RBD. (a) SERS mapping images of the positive sample (1) and different negative controls (2–5); (b) the extracted average Raman spectra from (a); and (c) the corresponding Raman intensity at 1603 cm<sup>-1</sup>.

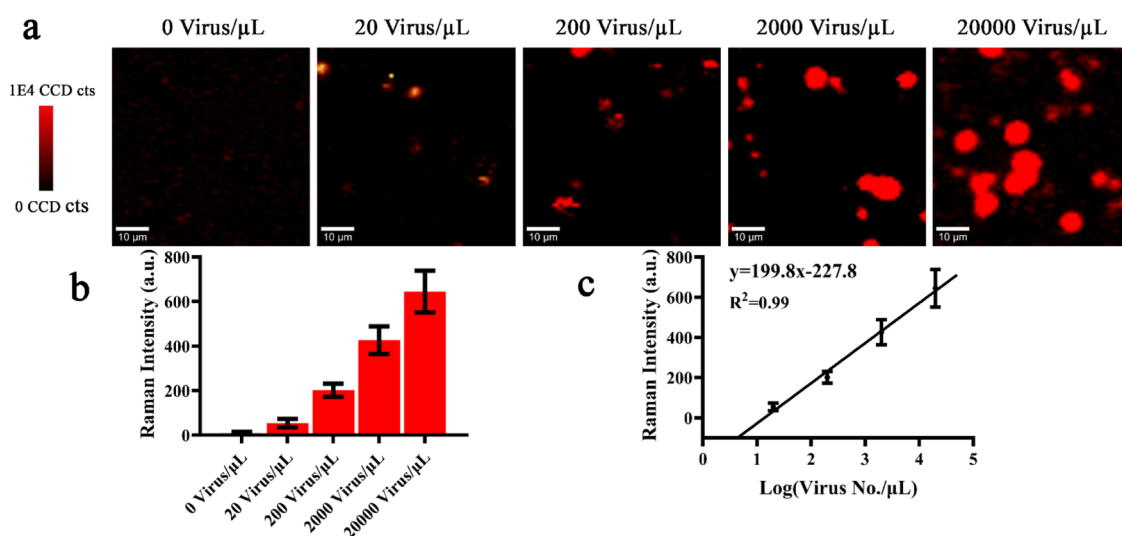


**Figure 7.** Sensitivity of SARS-CoV-2 detection. (a) Representative SERS mapping images; (b) Raman intensity at 1603 cm<sup>-1</sup> with different virus concentrations; and (c) the linear calibration curve between logarithmic virus concentration and Raman intensity.

five microelectrodes with a low coefficient of variation (CV) of 8.05% demonstrated the reproducible surface functionalization. Similarly, the nanobox surface functionalization with polyclonal antibodies via covalent binding also showed a desirable reproducibility with a CV lower than 10% (Figure S5).

To further investigate the performance of S309 nanoyeast-scFvs, we compared the soluble RBD detection on the designed platform using S309 nanoyeast-scFvs and S309 monoclonal antibodies as the capture affinity reagents. The comparable SERS intensities at 1603 cm<sup>-1</sup> achieved for S309 nanoyeast-scFvs and S309 monoclonal antibodies (Figure S6) indicated that the engineered scFvs can be employed as efficient alternatives for antibodies.

**Specificity for the Detection of Soluble RBD and SARS-CoV-2.** Due to the complexity of biological samples, the ability to specifically and reliably detect soluble RBD or SARS-

CoV-2 is thus critical to provide accurate diagnosis for effective control of disease spread. To demonstrate the specificity of soluble RBD detection, we challenged the platform with the positive and several negative control experiments (Figure 6). Specifically, using S309 nanoyeast-scFvs as a capture probe, we used soluble RBD (image 1) as the positive sample, PBS (image 2), 1% BSA (Figure S7), cell culture medium (Figure S7), and 20% human serum (Figure S7) as the negative samples. In addition, S309 nanoyeast-scFvs were further replaced with scFvs targeting other antigens as negative controls for soluble RBD detection, including m396 for SARS-CoV-1 (image 3),<sup>40</sup> E12 for dengue virus nonstructural protein 1 antigen (image 4), and 2F5 also for dengue virus nonstructural protein 1 antigen (image 5). As shown in the acquired SERS mapping images, due to the successful capture of soluble RBD, the positive sample (image 1) showed strong

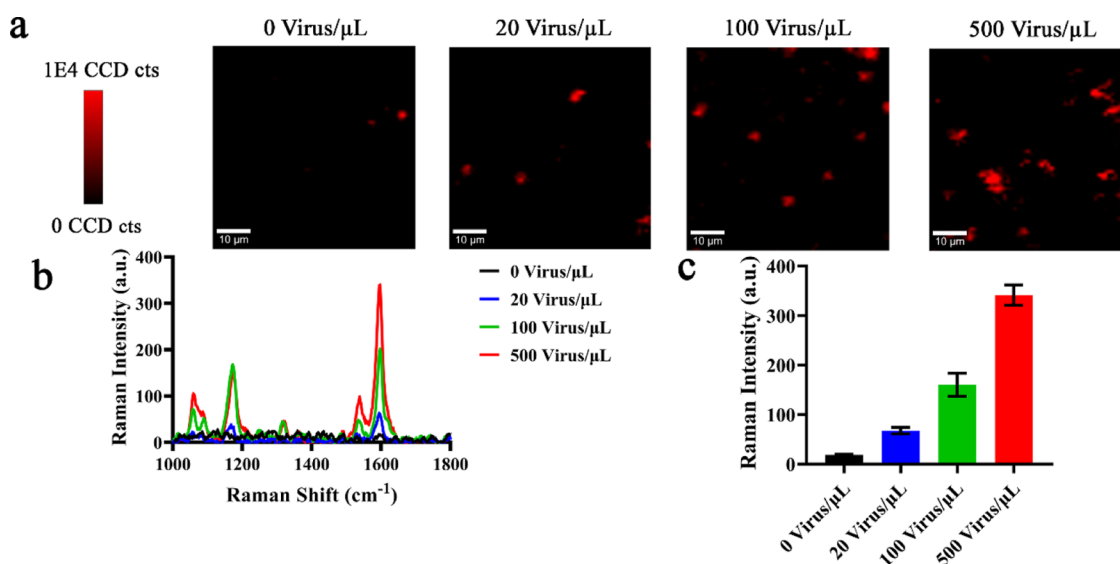


**Figure 8.** Simulated patient sample identification on the nanoyeast-scFv and ultrasensitive plasmonic nanobox-integrated nanomixing platform. (a) Representative SERS mapping images of healthy human saliva spiked with 0, 20, 100, and 500 virus/ $\mu\text{L}$ ; (b) the corresponding extracted average Raman spectra; and (c) Raman intensities at  $1603 \text{ cm}^{-1}$ . Error bars indicate the standard error of three replicates.

Raman signals. In contrast, all of the negative controls (image 2–5 and Figure S7) displayed negligible signals without being able to successfully and specifically capture soluble RBD. The extracted average Raman spectra (Figure 6b) and Raman intensities at  $1603 \text{ cm}^{-1}$  (Figure 6c) showed the consistent result with SERS mapping images, where the positive sample demonstrated much stronger signals than the negative controls. Therefore, the S309 nanoyeast-scFv-functionalized platform provided highly specific recognition of soluble RBD.

To further ensure the designed platform has the required specificity to detect SARS-CoV-2, we investigated the direct detection of the inactivated virus with the positive sample and multiple negative controls (Figure S8). As the SARS-CoV-2 was propagated in cell culture medium, the corresponding medium was employed as one of the negative control samples instead of PBS. Similar to the soluble RBD detection, we only observed the high Raman signals for the positive sample rather than the negative controls, which indicated the specificity for the detection of SARS-CoV-2.

Collectively, the designed platform had the high specificity for both soluble RBD and SARS-CoV-2 detection. In our current assay platform, the achieved high specificity can be largely attributed to S309 nanoyeast-scFvs that specifically recognize the unique viral RBD epitope.

**Sensitivity for the Detection of SARS-CoV-2.** To enable an early identification of infected patients and timely control of the virus transmission, a highly sensitive platform that can detect low concentrations of SARS-CoV-2 is desired. In an effort to study the sensitivity of the developed platform, we titrated different concentrations of SARS-CoV-2 into PBS and mapped the SERS signals for quantification. It is worth noting that the concentration of SARS-CoV-2 cultured in the cell line was predetermined by performing the standard RT-qPCR. With more SARS-CoV-2 captured on microelectrodes via S309 nanoyeast-scFvs, the obtained SERS mapping images showed an increasing proportion of SERS signal distributions (Figure 7a). In line with the SERS mapping images, the extracted average Raman intensity at  $1603 \text{ cm}^{-1}$  increased correspondingly with a higher virus concentration (Figure 7b). To

quantify the viral loads in patient samples, it is important to have an adequate detection range of the assay and quantitative relationship between SERS signal and virus concentration. In a logarithmic plot of the virus concentration, we found a strong correlation to the SERS intensities at  $1603 \text{ cm}^{-1}$  (Figure 7c) with a coefficient of correlation ( $R^2$ ) of 0.99. Furthermore, the assay's dynamic range covered 4 orders of magnitude, facilitating the quantification of virus in patients of various viral loads.

In our amplification-free assay, the developed platform was capable of detecting the virus to as low as 17 virus/ $\mu\text{L}$  calculated from three times the standard deviation of the blank signal, which was comparable to the recent amplification-based works for SARS-CoV-2 detection.<sup>8,41,42</sup> The achieved limit of detection met the clinical requirement for screening COVID-19 patients ( $\sim 100$  virus/ $\mu\text{L}$ ).<sup>43</sup> Such a low limit of detection on the nanoyeast-scFv-integrated SERS microarray platform can be attributed to the following three key features: the high affinity contributed from the engineered S309 nanoyeast-scFvs; the nanomixing enhanced molecular interactions on the microelectrodes; and the superbright SERS nanotags<sup>31</sup> binding to multiple RBD on the viral surfaces.

**Diagnosis of Simulated COVID-19 Patients.** Recent studies have demonstrated that human saliva specimens can be used as alternatives to nasopharyngeal swab samples in screening of COVID-19 patient with the appealing advantages of convenient self-sampling, better protection of health care workers, alleviating the potential discomfort suffered by the patients, and less variations of the detected SARS-CoV-2 levels.<sup>44,45</sup> We therefore utilized healthy human saliva specimens and spiked with SARS-CoV-2 to simulate healthy and COVID-19 people, respectively. To meet the clinically relevant requirement for patient screening (i.e., 100 virus/ $\mu\text{L}$ ) and test the influence of saliva matrix components, we prepared the simulated COVID-19 patient samples by spiking with a range of virus titers (i.e., 0, 20, 100, 500 virus/ $\mu\text{L}$ ).<sup>43,46</sup> Testing the healthy and simulated COVID-19 samples on the designed platform, the SERS mapping images and the extracted average Raman spectra (Figure 8) showed an increasing Raman

intensities with the increase of viral loads, indicating the good performance of the assay in saliva matrix components. Furthermore, the successful differentiation of 20 virus/ $\mu\text{L}$  in saliva from nonspiked saliva (i.e., 0 virus/ $\mu\text{L}$ ) suggested that the good detection limit can be maintained in real samples. Hence, the nanoyeast-scFv-integrated nanomixing SERS microarray platform has the potential of amplification-free identifying COVID-19 patients and the feasibility of being a useful tool in patient screening.

Compared to the gold standard RT-qPCR technique, our developed assay achieved a comparable limit of detection (i.e., 17 virus/ $\mu\text{L}$ ) with a faster processing ( $\sim 3$  h 25 min for 28 microelectrodes) but avoided sample pretreatments and the amplification bias. While commercial antigen tests enable rapid virus detection, our approach applied nanoyeast-scFvs as cost-effective, temperature-stable virus capture probes<sup>24</sup> and nanomixing-assisted Raman signal readout for highly sensitive COVID-19 screening.

## CONCLUSIONS

In summary, we developed the nanoyeast-scFv and ultra-sensitive plasmonic nanobox-integrated nanomixing assay for SARS-CoV-2 detection. The yeast display technology was used to rationally bioengineer a panel of scFvs targeting the RBD of SARS-CoV-2. The highest-avidity nanoyeast-scFvs, S309, was subsequently integrated on a microelectrode array device for specific virus capture. Significantly, the selective use of S309 nanoyeast-scFvs for virus detection achieved similar performance to the anti-RBD monoclonal antibody with the benefits of streamlined and cost-efficient production. To achieve amplification-free virus detection of as low as 17 virus/ $\mu\text{L}$ , we leveraged the superplasmonic nanostructures of gold–silver alloy nanoboxes to enhance the SERS signals. Furthermore, the employment of nanomixing on the microelectrode array facilitated the effective virus capture and nanobox-based SERS nanotag identification via enhancing the collisions among the viral particles, nanobox, and nanoyeast-scFv-conjugated microelectrode surface. In a proof-of-concept demonstration with the potential to detect less invasive samples, we successfully demonstrate our assay to detect SARS-CoV-2 in simulated human saliva at diagnostically relevant virus concentration that is required to identify newly infected patients (100 virus/ $\mu\text{L}$ ). By integrating the high adaptability of the nanoyeast-scFvs for specific recognizing virus in conjunction with the nanomixing and ultrasensitive nanostructure involved SERS for sensitive signal readout, we envision the developed amplification-free platform can overcome the bias issue and be a useful tool in the population-based COVID-19 screening.

## ASSOCIATED CONTENT

### Supporting Information

The Supporting Information is available free of charge at <https://pubs.acs.org/doi/10.1021/acs.analchem.1c01657>.

Flow cytometry analysis of S309 scFv display level and RBD binding on yeast cells; nanoflow cytometry measurement of S309 nanoyeast-scFvs; comparison of S309 nanoyeast-scFvs and S309 monoclonal antibodies; specificity study for SARS-CoV-2; and simulated patient sample identification (PDF)

## AUTHOR INFORMATION

### Corresponding Authors

**Alain Wuethrich** – Centre for Personalized Nanomedicine, Australian Institute for Bioengineering and Nanotechnology, The University of Queensland, Brisbane, QLD 4072, Australia; [orcid.org/0000-0001-9569-0478](https://orcid.org/0000-0001-9569-0478); Email: [a.wuethrich@uq.edu.au](mailto:a.wuethrich@uq.edu.au)

**Christopher B. Howard** – Centre for Personalized Nanomedicine, Australian Institute for Bioengineering and Nanotechnology, The University of Queensland, Brisbane, QLD 4072, Australia; [orcid.org/0000-0001-9797-8686](https://orcid.org/0000-0001-9797-8686); Email: [c.howard2@uq.edu.au](mailto:c.howard2@uq.edu.au)

**Matt Trau** – Centre for Personalized Nanomedicine, Australian Institute for Bioengineering and Nanotechnology, The University of Queensland, Brisbane, QLD 4072, Australia; School of Chemistry and Molecular Biosciences, The University of Queensland, Brisbane, QLD 4072, Australia; [orcid.org/0000-0001-5516-1280](https://orcid.org/0000-0001-5516-1280); Email: [m.trau@uq.edu.au](mailto:m.trau@uq.edu.au)

### Authors

**Junrong Li** – Centre for Personalized Nanomedicine, Australian Institute for Bioengineering and Nanotechnology, The University of Queensland, Brisbane, QLD 4072, Australia; [orcid.org/0000-0002-3777-2245](https://orcid.org/0000-0002-3777-2245)

**Selvakumar Edwardraja** – Centre for Personalized Nanomedicine, Australian Institute for Bioengineering and Nanotechnology, The University of Queensland, Brisbane, QLD 4072, Australia

**Richard J. Lobb** – Centre for Personalized Nanomedicine, Australian Institute for Bioengineering and Nanotechnology, The University of Queensland, Brisbane, QLD 4072, Australia

**Simon Puttick** – Probing Biosystems Future Science Platform, Commonwealth Scientific and Industrial Research Organization, Brisbane, QLD 4029, Australia

**Stephen Rose** – Probing Biosystems Future Science Platform, Commonwealth Scientific and Industrial Research Organization, Brisbane, QLD 4029, Australia

Complete contact information is available at: <https://pubs.acs.org/doi/10.1021/acs.analchem.1c01657>

### Notes

The authors declare no competing financial interest.

## ACKNOWLEDGMENTS

The authors acknowledge the funding from the ARC DP (160102836 and 140104006), which have significantly contributed to the current research. J.L. acknowledges the support from The Commonwealth Scientific and Industrial Research Organization Fellowship. A.W. thanks the National Health and Medical Research Council for funding (APP1173669). C.B.H. acknowledges funding support from the Advance Queensland Industry Research Fellowship-COVID19 (AQIRF104–2020-CV). The authors acknowledge researchers at ADHP, CSIRO, Geelong, for the preparation and RT-PCR analysis of  $\gamma$ -irradiated SARS-CoV-2, in particular Dr Alex McAuley for organization of  $\gamma$ -irradiated virus samples. They also acknowledge the facilities, and the scientific and technical assistance, of the Australian Microscopy & Microanalysis Research Facility at the Centre for Microscopy and Microanalysis, The University of Queensland. They appreciate

the technical and scientific guidance from the Queensland node of the Australian National Fabrication Facility (Q-ANFF) in confocal Raman mapping. They also acknowledge that elements of this research utilized equipment and services provided by the Queensland node of the National Biologics Facility (NBF). NBF is supported by Therapeutic Innovation Australia (TIA). TIA was supported by the Australian Government through the National Collaborative Research Infrastructure Strategy (NCRIS) program.

## REFERENCES

- (1) World Health Organization (WHO). COVID-19 Weekly Epidemiological Update, 2021. <https://www.who.int/publications/m/item/weekly-epidemiological-update-on-covid-19---23-march-2021>.
- (2) Huang, C.; Wang, Y.; Li, X.; Ren, L.; Zhao, J.; Hu, Y.; Zhang, L.; Fan, G.; Xu, J.; Gu, X.; Cheng, Z.; Yu, T.; Xia, J.; Wei, Y.; Wu, W.; Xie, X.; Yin, W.; Li, H.; Liu, M.; Xiao, Y.; et al. *Lancet* **2020**, *395*, 497–506.
- (3) He, X.; Lau, E. H. Y.; Wu, P.; Deng, X.; Wang, J.; Hao, X.; Lau, Y. C.; Wong, J. Y.; Guan, Y.; Tan, X.; Mo, X.; Chen, Y.; Liao, B.; Chen, W.; Hu, F.; Zhang, Q.; Zhong, M.; Wu, Y.; Zhao, L.; Zhang, F.; et al. *Nat. Med.* **2020**, *26*, 672–675.
- (4) Moghadas, S. M.; Fitzpatrick, M. C.; Sah, P.; Pandey, A.; Shoukat, A.; Singer, B. H.; Galvani, A. P. *Proc. Natl. Acad. Sci. U.S.A.* **2020**, *117*, 17513–17515.
- (5) Udugama, B.; Kadhiresan, P.; Kozlowski, H. N.; Malekjahani, A.; Osborne, M.; Li, V. Y. C.; Chen, H.; Mubareka, S.; Gubbay, J. B.; Chan, W. C. W. *ACS Nano* **2020**, *14*, 3822–3835.
- (6) Woo, C. H.; Jang, S.; Shin, G.; Jung, G. Y.; Lee, J. W. *Nat. Biomed. Eng.* **2020**, *4*, 1168–1179.
- (7) Ramachandran, A.; Huyke, D. A.; Sharma, E.; Sahoo, M. K.; Huang, C.; Banaei, N.; Pinsky, B. A.; Santiago, J. G. *Proc. Natl. Acad. Sci. U.S.A.* **2020**, *117*, 29518–29525.
- (8) Broughton, J. P.; Deng, X.; Yu, G.; Fasching, C. L.; Servellita, V.; Singh, J.; Miao, X.; Streithorst, J. A.; Granados, A.; Sotomayor-Gonzalez, A.; Zorn, K.; Gopez, A.; Hsu, E.; Gu, W.; Miller, S.; Pan, C.-Y.; Guevara, H.; Wadford, D. A.; Chen, J. S.; Chiu, C. Y. *Nat. Biotechnol.* **2020**, *38*, 870–874.
- (9) Ding, X.; Yin, K.; Li, Z.; Lalla, R. V.; Ballesteros, E.; Sfeir, M. M.; Liu, C. *Nat. Commun.* **2020**, *11*, No. 4711.
- (10) Arizti-Sanz, J.; Freije, C. A.; Stanton, A. C.; Petros, B. A.; Boehm, C. K.; Siddiqui, S.; Shaw, B. M.; Adams, G.; Kosoko-Thoroddsen, T.-S. F.; Kembell, M. E.; Uwanibe, J. N.; Ajogbasile, F. V.; Eromon, P. E.; Gross, R.; Wronka, L.; Caviness, K.; Hensley, L. E.; Bergman, N. H.; MacInnis, B. L.; Hapipi, C. T.; et al. *Nat. Commun.* **2020**, *11*, No. 5921.
- (11) Ma, P.; Meng, Q.; Sun, B.; Zhao, B.; Dang, L.; Zhong, M.; Liu, S.; Xu, H.; Mei, H.; Liu, J.; Chi, T.; Yang, G.; Liu, M.; Huang, X.; Wang, X. *Adv. Sci.* **2020**, *7*, No. 2001300.
- (12) Vogels, C. B. F.; Brito, A. F.; Wyllie, A. L.; Fauver, J. R.; Ott, I. M.; Kalinich, C. C.; Petrone, M. E.; Casanovas-Massana, A.; Catherine Muenker, M.; Moore, A. J.; Klein, J.; Lu, P.; Lu-Culligan, A.; Jiang, X.; Kim, D. J.; Kudo, E.; Mao, T.; Moriyama, M.; Oh, J. E.; Park, A.; et al. *Nat. Microbiol.* **2020**, *5*, 1299–1305.
- (13) Grant, B. D.; Anderson, C. E.; Williford, J. R.; Alonzo, L. F.; Glukhova, V. A.; Boyle, D. S.; Weigl, B. H.; Nichols, K. P. *Anal. Chem.* **2020**, *92*, 11305–11309.
- (14) Wang, C.; Yang, X.; Gu, B.; Liu, H.; Zhou, Z.; Shi, L.; Cheng, X.; Wang, S. *Anal. Chem.* **2020**, *92*, 15542–15549.
- (15) Chen, Z.; Zhang, Z.; Zhai, X.; Li, Y.; Lin, L.; Zhao, H.; Bian, L.; Li, P.; Yu, L.; Wu, Y.; Lin, G. *Anal. Chem.* **2020**, *92*, 7226–7231.
- (16) Norman, M.; Gilboa, T.; Ogata, A. F.; Maley, A. M.; Cohen, L.; Busch, E. L.; Lazarovits, R.; Mao, C.-P.; Cai, Y.; Zhang, J.; Feldman, J. E.; Hauser, B. M.; Caradonna, T. M.; Chen, B.; Schmidt, A. G.; Alter, G.; Charles, R. C.; Ryan, E. T.; Walt, D. R. *Nat. Biomed. Eng.* **2020**, *4*, 1180–1187.
- (17) Bradbury, A.; Plücker, A. *Nature* **2015**, *518*, No. 27.
- (18) Marx, V. *Nat. Methods* **2013**, *10*, 703–707.
- (19) Dinnes, J.; Deeks, J. J.; Berhane, S.; Taylor, M.; Adriano, A.; Davenport, C.; Dittrich, S.; Emperador, D.; Takwoingi, Y.; Cunningham, J.; Beese, S.; Domen, J.; Dretzke, J.; Ferrante di Ruffano, L.; Harris, I. M.; Price, M. J.; Taylor-Phillips, S.; Hoof, L.; Leeflang, M. M.; McInnes, M. D.; et al. *Cochrane Database Syst. Rev.* **2021**, *3*, No. Cd013705.
- (20) Zhang, W.; Du, R.-H.; Li, B.; Zheng, X.-S.; Yang, X.-L.; Hu, B.; Wang, Y.-Y.; Xiao, G.-F.; Yan, B.; Shi, Z.-L. *Emerging Microbes Infect.* **2020**, *9*, 386–389.
- (21) Wuethrich, A.; Sina, A. A. I.; Ahmed, M.; Lin, T.-Y.; Carrascosa, L. G.; Trau, M. *Nanoscale* **2018**, *10*, 10884–10890.
- (22) Koo, K. M.; Dey, S.; Trau, M. *ACS Sens.* **2018**, *3*, 2597–2603.
- (23) Koo, K. M.; Dey, S.; Trau, M. *Small* **2018**, *14*, No. 1704025.
- (24) Grewal, Y. S.; Shiddiky, M. J. A.; Mahler, S. M.; Cangelosi, G. A.; Trau, M. *ACS Appl. Mater. Interfaces* **2016**, *8*, 30649–30664.
- (25) Grewal, Y. S.; Shiddiky, M. J. A.; Gray, S. A.; Weigel, K. M.; Cangelosi, G. A.; Trau, M. *Chem. Commun.* **2013**, *49*, 1551–1553.
- (26) Chao, G.; Lau, W. L.; Hackel, B. J.; Sazinsky, S. L.; Lippow, S. M.; Wittrup, K. D. *Nat. Protoc.* **2006**, *1*, 755–768.
- (27) Li, J.; Wang, J.; Grewal, Y. S.; Howard, C. B.; Raftery, L. J.; Mahler, S.; Wang, Y.; Trau, M. *Anal. Chem.* **2018**, *90*, 10377–10384.
- (28) Zhang, Z.; Wang, J.; Shanmugasundaram, K. B.; Yeo, B.; Möller, A.; Wuethrich, A.; Lin, L. L.; Trau, M. *Small* **2020**, *16*, No. 1905614.
- (29) Gai, S. A.; Wittrup, K. D. *Curr. Opin. Struct. Biol.* **2007**, *17*, 467–473.
- (30) Walker, R. S. K.; Pretorius, I. S. *Genes* **2018**, *9*, No. 340.
- (31) Li, J.; Wuethrich, A.; Sina, A. A. I.; Cheng, H.-H.; Wang, Y.; Behren, A.; Mainwaring, P. N.; Trau, M. *Nat. Commun.* **2021**, *12*, No. 1087.
- (32) Lane, L. A.; Qian, X.; Nie, S. *Chem. Rev.* **2015**, *115*, 10489–10529.
- (33) Chen, L.; Ying, B.; Song, P.; Liu, X. *ACS Appl. Mater. Interfaces* **2019**, *6*, No. 1901346.
- (34) Li, J.; Koo, K. M.; Wang, Y.; Trau, M. *Small* **2019**, *15*, No. 1904689.
- (35) Pinto, D.; Park, Y.-J.; Beltramello, M.; Walls, A. C.; Tortorici, M. A.; Bianchi, S.; Jaconi, S.; Culap, K.; Zatta, F.; De Marco, A.; Peter, A.; Guarino, B.; Spreafico, R.; Cameroni, E.; Case, J. B.; Chen, R. E.; Havenar-Daughton, C.; Snell, G.; Telenti, A.; Virgin, H. W.; et al. *Nature* **2020**, *583*, 290–295.
- (36) Brouwer, P. J. M.; Caniels, T. G.; van der Straten, K.; Snitselaar, J. L.; Aldon, Y.; Bangaru, S.; Torres, J. L.; Okba, N. M. A.; Claireaux, M.; Kerster, G.; Bentlage, A. E. H.; van Haaren, M. M.; Guerra, D.; Burger, J. A.; Schermer, E. E.; Verheul, K. D.; van der Velde, N.; van der Kooij, A.; van Schooten, J.; van Breemen, M. J.; et al. *Science* **2020**, *369*, 643–650.
- (37) Huang, J.; Huang, H.; Wang, D.; Wang, C.; Wang, Y. *Clin. Transl. Med.* **2020**, *10*, No. e184.
- (38) Wu, Y.; Wang, F.; Shen, C.; Peng, W.; Li, D.; Zhao, C.; Li, Z.; Li, S.; Bi, Y.; Yang, Y.; Gong, Y.; Xiao, H.; Fan, Z.; Tan, S.; Wu, G.; Tan, W.; Lu, X.; Fan, C.; Wang, Q.; Liu, Y.; et al. *Science* **2020**, *368*, 1274–1278.
- (39) Wang, Y.; Yan, B.; Chen, L. *Chem. Rev.* **2013**, *113*, 1391–1428.
- (40) Prabakaran, P.; Gan, J.; Feng, Y.; Zhu, Z.; Choudhry, V.; Xiao, X.; Ji, X.; Dimitrov, D. S. *J. Biol. Chem.* **2006**, *281*, 15829–15836.
- (41) Yu, S.; Nimse, S. B.; Kim, J.; Song, K.-S.; Kim, T. *Anal. Chem.* **2020**, *92*, 14139–14144.
- (42) Pang, B.; Xu, J.; Liu, Y.; Peng, H.; Feng, W.; Cao, Y.; Wu, J.; Xiao, H.; Pabbaraju, K.; Tipples, G.; Joyce, M. A.; Saffran, H. A.; Tyrrell, D. L.; Zhang, H.; Le, X. C. *Anal. Chem.* **2020**, *92*, 16204–16212.
- (43) Larremore, D. B.; Wilder, B.; Lester, E.; Shehata, S.; Burke, J. M.; Hay, J. A.; Tambe, M.; Mina, M. J.; Parker, R. *Sci. Adv.* **2021**, *7*, No. eabd5393.
- (44) Wyllie, A. L.; Fournier, J.; Casanovas-Massana, A.; Campbell, M.; Tokuyama, M.; Vijayakumar, P.; Warren, J. L.; Geng, B.; Muenker, M. C.; Moore, A. J.; Vogels, C. B. F.; Petrone, M. E.; Ott, I.

M.; Lu, P.; Venkataraman, A.; Lu-Culligan, A.; Klein, J.; Earnest, R.; Simonov, M.; Datta, R.; et al. *N. Engl. J. Med.* **2020**, *383*, 1283–1286.

(45) Ning, B.; Yu, T.; Zhang, S.; Huang, Z.; Tian, D.; Lin, Z.; Niu, A.; Golden, N.; Hensley, K.; Threeton, B.; Lyon, C. J.; Yin, X.-M.; Roy, C. J.; Saba, N. S.; Rappaport, J.; Wei, Q.; Hu, T. Y. *Sci. Adv.* **2021**, *7*, No. eabe3703.

(46) Fozouni, P.; Son, S.; de León Derby, M. D.; Knott, G. J.; Gray, C. N.; D'Ambrosio, M. V.; Zhao, C.; Switz, N. A.; Kumar, G. R.; Stephens, S. I. *Cell* **2020**, *184*, 323–333.